Applications in Energy and Combustion Science 23 (2025) 100362

Contents lists available at ScienceDirect

Applications in Energy and Combustion Science

journal homepage: www.sciencedirect.com/journal/applications-in-energy-and-combustion-science

Sustainable hydrogen production from waste plastics via staged chemical looping gasification with iron-based oxygen carrier

Zongqiang Ren [a,b], Zhenghui Gao [b], Zhenliang Guo [b], Peiwen Liu [a], Dingding Yao [a,*]

[a] College of Engineering, Huazhong Agricultural University, Wuhan 430070, China
[b] School of Engineering, Cardiff University, Cardiff CF24 3AA, United Kingdom

ARTICLE INFO

Keywords:
Waste plastics
Hydrogen production
Staged chemical looping gasification
Iron oxygen carrier

ABSTRACT

Thermo-chemical conversion of waste plastics offers a sustainable strategy for integrated waste management and clean energy generation. To address the challenges of low gas yield and rapid catalyst deactivation due to coking in conventional gasification processes, an innovative three-stage chemical looping gasification (CLG) system specifically designed for enhanced hydrogen-rich syngas production was proposed in this work. A comparative analysis between conventional gasification and the staged CLG system were firstly conducted, coupled with online gas analysis for mechanistic elucidation. The influence of Fe/Al molar ratios in oxygen carriers and their cyclic stability were systematically examined through multicycle experiments. Results showed that the three-stage CLG in the presence of Fe1Al2 demonstrated exceptional performance, achieving 95.23 mmol/$g_{plastic}$ of H_2 and 129.89 mmol/$g_{plastic}$ of syngas respectively, representing 1.32-fold enhancement over conventional method. And the increased H_2/CO ratio (2.68–2.75) reflected better syngas quality via water-gas shift. Remarkably, the oxygen carrier maintained nearly 100 % of its initial activity after 7 redox cycles, attributed to the incorporation of Al_2O_3 effectively mitigating sintering and phase segregation through metal-support interactions. These findings establish a three-stage CLG configuration with Fe-Al oxygen carriers as an efficient platform for efficient hydrogen production from waste plastics, contributing to sustainable waste valorisation and carbon-neutral energy systems.

1. Introduction

Plastics are a class of versatile materials have significantly improved the quality of life for billions of people worldwide. However, the growing demand for plastic products in modern society has led to a substantial increase in plastic waste generation [1]. The excessive use and global distribution of single-use plastic bags (exceeding one trillion per year) have been identified as a key contributor to environmental degradation, with documented impacts on human health, terrestrial and aquatic pollution, and inefficiencies in waste management systems [2,3]. In addition, recurring public health challenges, such as seasonal influenza, have led to a continued increase in the consumption of plastic products, especially single-use items [4]. Although recent years have seen improvements in plastic waste collection and recycling efforts, around 69 % of post-consumer plastic waste was still sent to landfill or incineration [5,6]. To achieve a sustainable plastic circular economy, innovative technologies are urgently needed to convert and upcycle plastic waste into valuable products [7,8].

Hydrogen has emerged as a promising clean energy carrier, expected to play a pivotal role in future low-emission and sustainable energy systems [9–11]. Waste plastics can serve as a feedstock for hydrogen-rich syngas production through thermal-chemical processes such as pyrolysis, gasification, and catalytic reforming, offering a viable pathway for both waste valorisation and clean energy generation [12–14]. Over the past decade, growing interest has emerged in the conversion of waste plastics into hydrogen and syngas, and various thermochemical systems have been developed for this purpose. For example, Barbarias et al. [15] designed a continuous system combining a conical spouted bed reactor and a fluidised bed to process high-density polyethylene. Dou et al. [16] integrated a fluidised-bed gasification system integrated with sorption-enhanced process, where CaO adsorption increased hydrogen concentration to 88.4 vol %. Saad and Williams [17] employed a pyrolysis-catalytic reforming system, and Yao et al. [18] further demonstrated the feasibility of the hydrogen and syngas production process from waste plastics.

Chemical looping gasification (CLG) has recently emerged as a

* Corresponding author.
E-mail address: dingdingyao@mail.hzau.edu.cn (D. Yao).

https://doi.org/10.1016/j.jaecs.2025.100362
Received 21 June 2025; Received in revised form 27 July 2025; Accepted 5 August 2025
Available online 7 August 2025

promising alternative for hydrogen production from carbonaceous feedstocks [19]. Unlike conventional gasification systems where feedstock is co-processed with gasification agents and catalysts in a single reactor – inevitably causing overlapping reaction zones, elevated tar formation and syngas dilution [20] – CLG spatially decouples gasification and oxygen carrier regeneration, enhancing gasification efficiency with elevated H_2 concentration in syngas, while also reducing tar, improving carbon conversion, and increasing energy efficiency compare to traditional methods [21]. A key feature of CLG is its use of lattice oxygen through redox reactions rather than molecular oxygen, enabling partial oxidation which enhances syngas yield and quality [22]. In addition, CLG is associated with several operational advantages, including higher gas calorific value, reusing of oxygen carriers, and improved overall system efficiency and cost-effectiveness [23]. Recent studies have further confirmed these advantages. For example, lignite-based CLG has been shown to increase hydrogen concentration by over 90 %, significantly improving the overall calorific value of product gas [24]. High gasification efficiencies have also been reported, with carbon conversion rates reaching up to 93.03 % and syngas selectivity exceeding 70 % under optimised conditions [25]. Moreover, overall hydrogen energy efficiency in CLG systems has been reported as high as 77.9 %, alongside near-complete fuel conversion, highlighting the potential of CLG to achieve both clean and efficient energy production [26].

Among various oxygen carriers applied in CLG process, Fe and Ni based catalysts have been extensively investigated due to their capacity to cleave C—C and C—H bonds [27–29]. However, Ni-based catalysts are limited by their inability to effectively decompose steam into hydrogen. In contrast, Fe-based catalysts not only reduce steam to produce high-purity hydrogen by water splitting reaction [30], but they have been also identified as the most promising candidates because low cost, abundant natural source, high oxygen storage, and syngas selectivity [31,32]. Despite these advantages, iron-based catalysts often suffer from deactivation due to sintering at high temperatures over multiple cycles [33]. To address this limitation, incorporation with supports such as Al_2O_3, MgO, CeO_2, and SiO_2 are commonly introduced to form composite catalysts that inhibit sintering and improve redox stability [34,35]. Among them, Fe_2O_3/Al_2O_3 (Fe-Al) composites have shown superior catalytic performance and cycle durability. For instance, Dharanipragada et al. [36] reported that Al_2O_3 facilitates Fe-Al spinel formation, improving structural integrity during long-term operation. Zhen et al. [30] demonstrated that the addition of inert alumina can effectively inhibit the collapse of the spatial structure and sintering of the Fe and evidently improve its reactivity and recyclability. Similarly, Zhu et al. [37] also suggested that the Fe-Al catalyst retained strong redox activity over 15 consecutive cycles.

Building upon the aforementioned insights, the integration of CLG with plastic valorisation emerges as a technologically viable pathway for waste mitigation and hydrogen energy synthesis. This is particularly critical for plastic feedstocks, which undergo complex degradation pathways involving rapid devolatilization and significant tar evolution, thereby compromising operational stability in conventional CLG configurations. Whereas conventional processes suffer from irreversible oxygen carrier deactivation due to mixed feeding of reactants, a rationally designed three-stage CLG is introduced in this work. The innovation lies in its spatially/temporally stepwise reaction sequence: (1) plastic pyrolysis coupled with OCs-mediated cracking, (2) steam reforming facilitated by reduced OCs, and (3) OC reoxidation. Fe-Al based oxygen carrier catalyst with varying Fe/Al ratios were synthesised and evaluated in relation to hydrogen yield and gas production. The reaction mechanisms and oxygen carrier structural evolution were also systematically investigated through a series of characterisation and performance tests.

Table 1
Ultimate and proximate analysis of disposable masks.

Ultimate analysis (wt. %)					Proximate analysis (wt. %)		
C	H	O	N	S	Moisture	Volatile	Ash
80.36	11.15	8.31	0.14	0.04	0.11	98.24	1.65

2. Materials and methods

2.1. Sample preparation

In this work, disposable masks - a representative category of post-consumer plastic waste - were selected as the model feedstock, sourcing from a local pharmacy store in Wuhan. For sample preparation, the nose clip made of metal was removed from the mask while the remaining mask material was cut into pieces of 2–3 mm. The main components include polypropylene (PP), polyethylene (PE) and nylon. The ultimate analysis of feedstock was determined by an Elementar Vario EL III. As shown in Table 1, the main elements in the mask were C, H and O. The proximate analysis was based on ASTM standards E790, E897 and E830 to get the moisture, volatile and ash content, respectively. Results showed that the volatile matter in the mask accounted for the largest proportion, up to 98.24 wt. %, while the moisture and ash took a very small percentage.

Fe-Al oxygen carriers (Fe-Al refers to the mixed oxide of Fe and Al) with different Fe to Al molar ratio (Fe/Al, Fe:Al=1:4, 1:2, 1:1 and 2:1, denoted as Fe1Al4, Fe1Al2, Fe1Al1 and Fe2Al1, respectively) were synthesised by wet impregnation method. Specifically, a certain amount of $Fe(NO_3)_3{\cdot}9H_2O$ was dissolved in 100 ml deionised water followed by mixing with activated alumina powders. The mixtures were then uniformly stirred under a magnetic stirring apparatus at 90 °C until it became a slurry. The obtained precursors were dried overnight and calcined at 850 °C in air atmosphere for 4 h. The resultant catalyst powders in the size of 50–250 μm were stored in desiccator for further experiment. All chemical reagents used in this work were purchased from Shanghai Aladdin Biochemical Technology Co., Ltd, China.

2.2. Experimental procedure for hydrogen production

The gasification experiments were performed in a fixed bed system as displayed in Fig. 1. The entire reaction system was mainly composed of gas (steam) feeding system, a stainless steel tube reactor (750 × ø50 mm), heating and temperature controlling system, volatiles condenser and products analysis system. A three staged reaction procedure (CLG) was applied to enhance the hydrogen production. For each experiment, Stage-I: 1 g of catalyst was firstly loaded in the middle of lower bed where the catalysis temperature was heated to 800 °C and kept stable. 1 g of feedstock was then introduced into the upper bed where pyrolysis took place from room temperature to 600 °C at 30 °C/min. Then the experiment was continued for another 30 min at 600 °C to ensure the completion of all reactions. Stage-II: Steam was introduced to the lower bed reactor for catalytic steam reforming process at 6 ml/h for 20 min. Stage-III: The spent catalysts were oxidised in-situ inside the lower bed in 200 ml/min air atmosphere for 10 min to return to the oxide state for the next run. Both stage II and III were held at 800 °C during the experiment. For comparison, the controlled trial was performed by using a single stage procedure, that is, steam was supplied during the pyrolysis-catalysis process, which is the most common method used for plastic gasification in literatures. All operational parameters for the controlled trial including temperature and steam feeding amount kept the same as the staged procedure. During the experiment, high purity nitrogen was continuously supplied at 100 ml/min as the inert carrier gas and internal gas agent for gas yield calculation. The non-condensable gas generated during each stage was collected by Tedlar gas sampling bag and was further analysed by gas chromatography (GC).

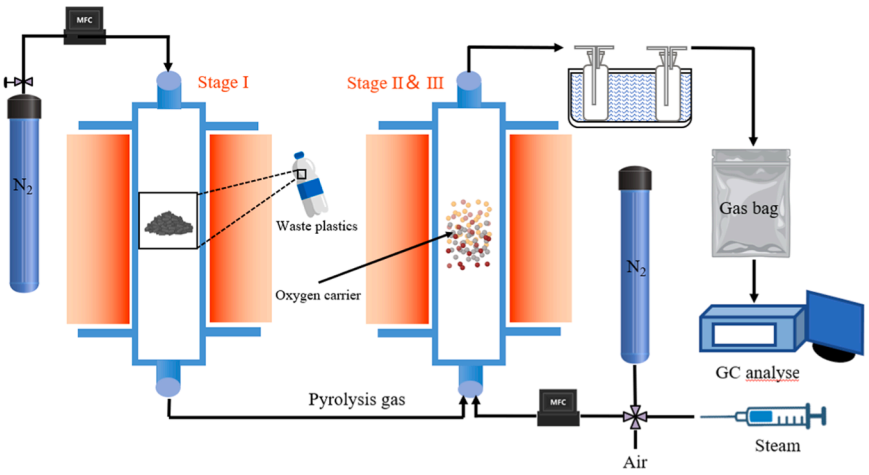

Fig. 1. Schematic of the staged CLG system.

The solid residues including the spent catalysts were cooled down and sampled for further analysis. A bubble film flowmeter was employed at the system outlet prior to each experiment to verify gas-tight integrity. Each experiment was repeated at least twice for data reliability.

2.3. Product analysis and characterisations

The gaseous product was analysed by a packed column FULI 9790-II GC. Permanent gases including H_2, CO_2, O_2, N_2 and CO were detected by TCD while hydrocarbons (C_1—C_4) were measured by FID using Ar as carrier gas. The gas composition was calibrated by the standard gas, and the yield of each gas was calculated based on the gas composition from GC in combination with the flow of nitrogen (R1). The yield of the liquid product was calculated as the mass difference of condenser before and after the reaction. The amount of carbon deposit was determined by the temperature programmed oxidation (TPO) of spent catalysts. The specimen was firstly dried at 100 °C for 10 min then was heated to 850 °C at a temperature ramp rate of 15 °C/min in air atmosphere.

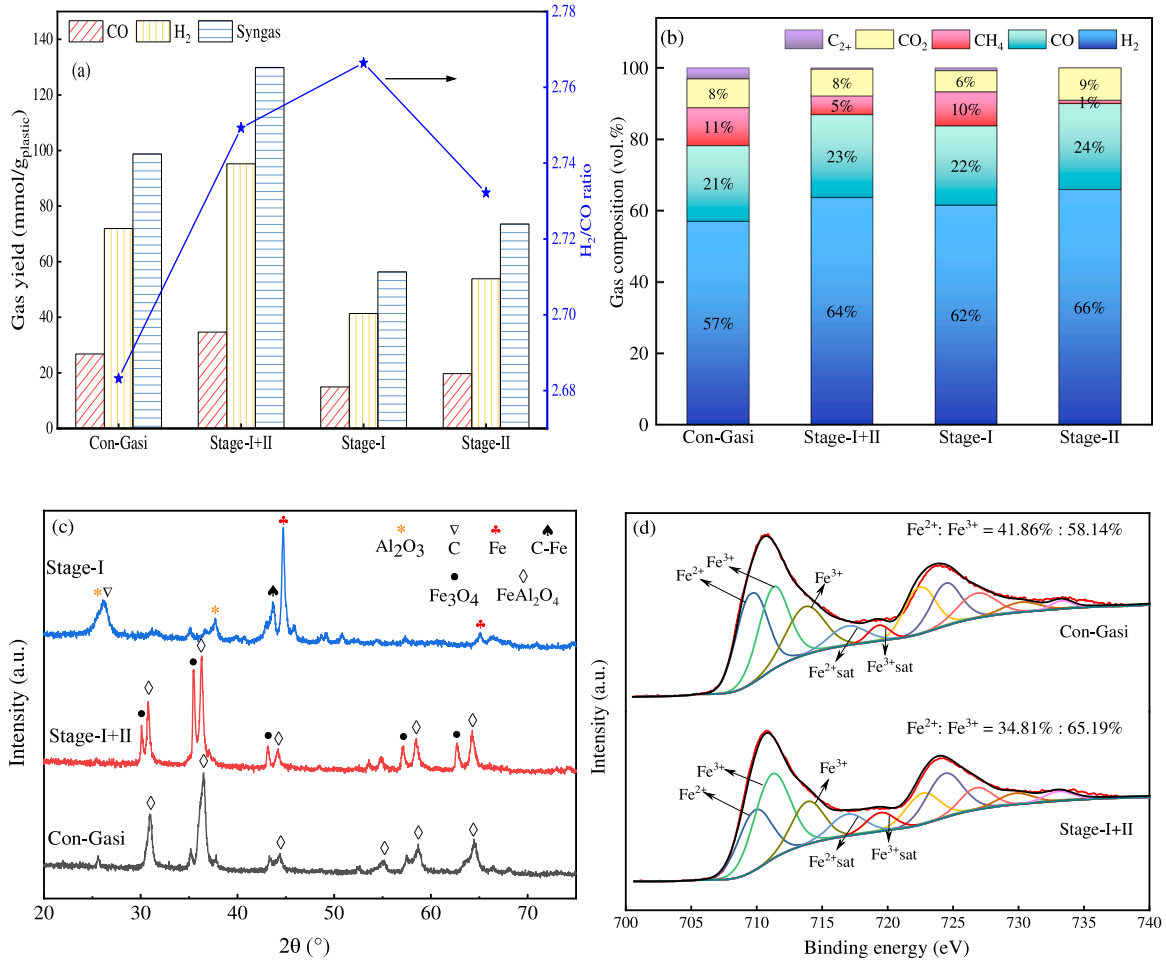

Fig. 2. Comparation of different kinds of steam gasification:(a) gas yield, (b) gas composition, (c) XRD results and (d) XPS results.

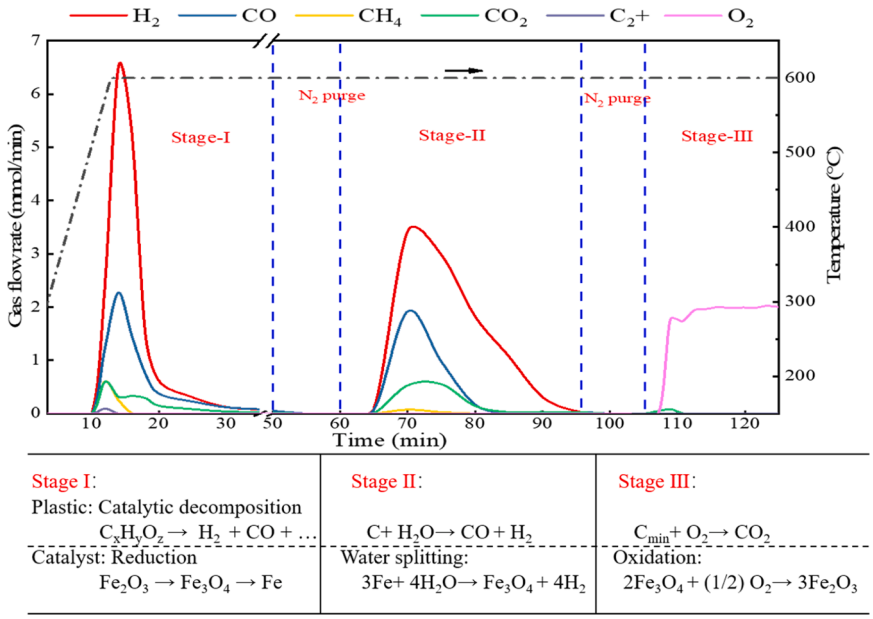

Fig. 3. The evolution of gas products in the staged CLG process.

$$Y_{gas}(\text{mmol}/\text{g}) = \left(C_{gas} \times Q_{N_2} \times t\right)/\left(C_{N_2} \times m_{plastic} \times 22.4\right) \quad \text{(R1)}$$

The concentrations of gaseous products and nitrogen were denoted as C_{gas} and C_{N_2}, while Q_{N_2}, t, and $m_{plastic}$ represented the nitrogen flow rate, reaction time, and waste plastic mass, respectively. The yield of syngas referred to the sum of hydrogen and carbon monoxide yields.

The crystalline phases of catalysts were identified by X-ray diffraction (XRD) analysis using a Bruker D8 Advance diffractometer with Cu K_α radiation (40 kV, 40 mA) and the scanning speed was 10 °/min. X-ray photoelectron spectroscopy (XPS) measurements were carried out in a Thermo Scientific K-Alpha system equipped with a monochromatic Al Kα X-ray source (1486.6 eV) to identify surface elements, quantify their concentrations, and analyse their oxidation states. A field emission scanning electron microscope (FE-SEM) was used to observe the morphology of fresh and spent catalysts. Before the observation, samples were sputter-coated with a thin layer of platinum to ensure surface conductivity. The specific surface areas of catalysts were determined by the Brunauer-Emmett-Teller (BET) method and the total pore volume, and the average pore size were obtained from the BJH method. Before the measurements, about 0.2 g catalyst were degassed in vacuum at 300 °C for 6 h to remove moisture and physically adsorbed components.

The H_2/CO ratio and CO selectivity were defined by the following (R2) and (R3), where F_i is the molar flow rate of different gaseous products during the reaction.

$$H_2/\text{CO ratio} = F_{H_2}/F_{CO} \quad \text{(R2)}$$

$$\text{CO selectivity} = F_{CO}/(F_{CO} + F_{CO_2}) \times 100\% \quad \text{(R3)}$$

3. Results and discussion

3.1. CLG in comparison to conventional gasification

The performance of the three-stage CLG for hydrogen-rich syngas production from waste plastic was investigated and compared with the conventional steam gasification (Con-Gasi). Both experiments were performed at 800 °C and steam feeding rate of 6 ml/h in the presence of Fe1Al2 oxygen carrier. The importance of catalyst in the reaction system was also verified by performing a non-catalytic trial. Fig. S1 shows that the introduction of catalyst significantly increased the production of small molecule gases such as H_2, CO and CO_2 with the consumption in heavy hydrocarbon gases (CH_4 and C_{2+}: C_2H_6, C_2H_4, C_3H_8, C_3H_6, C_4H_{10}, C_4H_8). This is because the volatilisation produced by pyrolysis reacts with the catalyst to promote the conversion of macromolecular compounds to small molecular gases [38]. Fig. 2(a) shows that in case of the conventional steam gasification, H_2 and CO reached 71.95 mmol/g and 26.81 mmol/g, contributing to a total syngas production of 98.76 mmol/g. In contrast, the CLG process achieved a significantly higher syngas yield of 129.90 mmol/g - an increase of 31.53 %. Notably, the increased H_2/CO ratio (from 2.68 to 2.75) demonstrates enhanced syngas quality due to improved water-gas shift activity, which also contributes to the reduction of carbon deposition and prolongation OCs' lifespan [39]. These results clearly demonstrate the superior reforming efficiency and hydrogen selectivity of the CLG process. In comparison with published studies on plastic gasification, Lazzarotto et al. [40] investigated the steam gasification of plastic wastes recovered from the municipal solid waste, hydrogen yield of 84.69 mmol/g was obtained. Yao et al. [18] used an in-line catalytic reforming system for HDPE steam reforming, and hydrogen/syngas yields reached 66.09 mmol/g and 100.72 mmol/g. The present study not only surpasses these reported values but also validates the advantage of integrating a staged reforming system via CLG.

In terms of gas composition, as shown in Fig. 2(b), H_2 accounted for the largest proportion in the gaseous mixture, followed by CO and other hydrocarbon gases. The significantly lower concentrations of hydrocarbon gases in CLG compared to Con-Gasi suggest more effective conversion of carbonaceous intermediates into syngas, primarily through enhanced steam reforming reactions. These findings highlight the thermochemical advantages of CLG in maximising hydrogen-rich syngas yield while minimising tar and hydrocarbon by-products, making it a highly promising strategy for advanced plastic waste valorisation.

The mineral composition and chemical states of the oxygen carrier from both Con-Gasi and CLG staged process were characterised in Fig. 2 (c-d). In Fig. 2(c), $FeAl_2O_4$ was identified as the predominant iron crystalline phase after gasification. XPS results in Fig. 2(d) show that the proportions of $Fe^{2+}$and Fe^{3+} in Con-Gasi process were 41.86 % and 58.14 %, respectively. This mixed valence distribution is attributed to the influence of oxygen from steam. However, the CLG process demonstrated a markedly different chemical environment. The XRD results show that almost all iron oxides were reduced to metallic Fe during the stage-I. This is because the staged steam reforming process ensures strongly reducing conditions that enhance iron reduction in the first step reaction. Although metallic Fe^0 was not explicitly resolved in

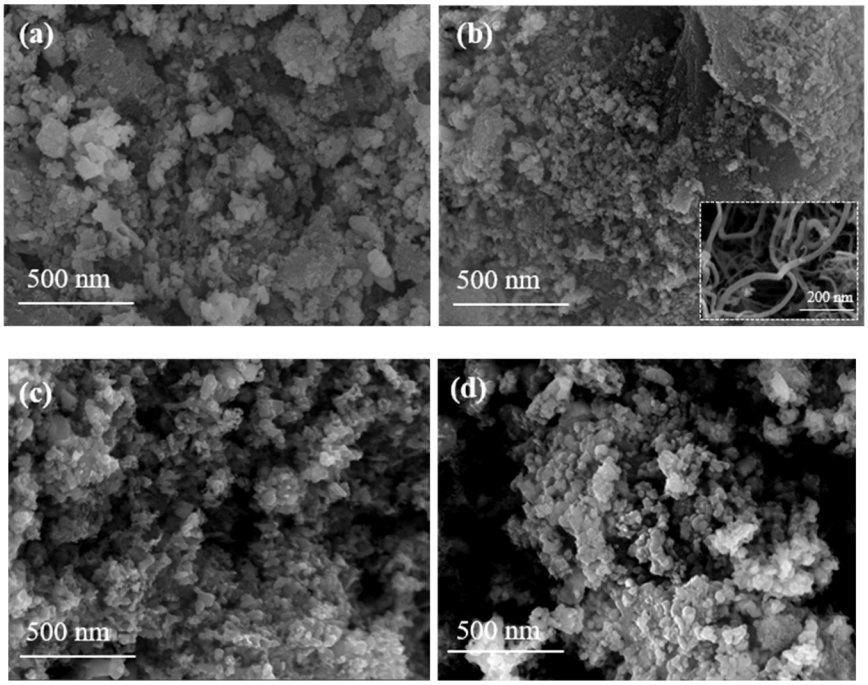

Fig. 4. SEM micrographs of (a) fresh catalyst, catalyst sample after (b) Stage-I, (c) Stage-II and (d) Stage-III.

the Fe 2p region due to its overlap with Fe^{2+} signals, the shift in the Fe oxidation state profile - together with the reaction environment - suggests enhanced redox activity and partial reduction of iron species during Stage-I, followed by reoxidation in Stage-II. This cycling is characteristic of CLG operation and reflects the dynamic redox behaviour of the Fe-based oxygen carrier under alternating reducing and oxidising atmospheres.

The hydrogen production capacity of steam reforming also depends on the reduction state of the catalyst after the reduction reaction. The lower the reduction degree, the stronger the hydrogen production capacity [30]. From XRD analysis of the spent catalyst, more Fe_3O_4 was identified on CLG process after stage II. Indicating that more iron species participate in the water splitting reaction under this condition. And most of the crystal components were $FeAl_2O_4$ in Con-Gasi process, which was stable and difficult to be reduced and re-used for subsequent recycling. In addition, there is a competitive reaction between steam reforming and catalytic pyrolysis in Con-Gasi process, and part of steam fails to participate in the reaction. However, in the CLG process, steam is introduced during the second-step reaction. This allows for a buffering effect, where only the reduced metallic Fe and carbon deposits react with the steam. This selective reaction promotes the directed conversion of water vapor into syngas.

3.2. Overview of the CLG procedure

The evolution of gas products during the CLG process was monitored to elucidate the reaction mechanism underpinning the staged production of hydrogen-rich syngas, as shown in Fig. 3. The reaction of stage-I can be divided into 3 steps: (1) initial pyrolysis: in the 10th (about 500 °C) minute, feedstock was rapidly thermally cracked to generate a large amount of pyrolysis gas (R4). Since the oxygen content in disposable masks is limited and the oxygen-containing groups are present only in the side chains of plastic polymers, they readily reacted at the initial stage of the pyrolysis process, leading to the early detection of CO and CO_2 [38,41]; (2) oxygen carrier reduction/oxidative reforming: as the reaction progressed, the reducing pyrolysis gas would react with the oxygen supplied by the iron-based catalyst (R5-R7). The second step witnessed a large CO_2 generation, which was due to the high oxygen content and strong oxidation ability in the catalyst, and the C atoms in the pyrolysis gas would be completely oxidised to CO_2 and the H atoms would be oxidised to H_2O. As the oxygen in the catalyst was gradually consumed, the CO_2 generation rate decreased. Meanwhile, reducing gases such as CH_4 were partially oxidised to CO, resulting in a noticeable increase in CO concentration; (3) deep reforming and metallic Fe activation: with the complete reduction of Fe_2O_3, the presence of metallic Fe and high temperature facilitated the secondary cracking of hydrocarbons such as CH_4 and C_{2+} compounds, leading to the formation of carbon and H_2 (R8) [20]. Additionally, metallic Fe catalysed the decomposition of tar, producing H_2, H_2O and various hydrocarbons (R9) [42].

$$C_xH_yO_z \rightarrow H_2 + CO + CO_2 + CH_4 + C_{2+} + \text{Tar} + \text{Char} \quad \text{(R4)}$$

$$C_xH_y + [O] \rightarrow CO_2 + H_2O \quad \text{(R5)}$$

$$H_2 + [O] \rightarrow H_2O \quad \text{(R6)}$$

$$CH_4 + 3[O] \rightarrow CO + 2H_2O \quad \text{(R7)}$$

$$C_xH_y \rightarrow xC + (y/2)H_2 \quad \text{(R8)}$$

$$\text{Tar} \rightarrow H_2 + CO + CO_2 + H_2O + C_xH_y \quad \text{(R9)}$$

Upon completion of stage-I, steam was introduced into the reactor to initiate stage-II. During this stage, solid carbon deposited in the stage-I and the reduced iron species would undergo reforming reaction with the steam to produce high-purity H_2 and CO, thereby further improving the concentration of hydrogen and syngas in the entire gasification process. Initially, steam preferentially reacted with the carbon deposits on the surface of the catalyst (R10), initiating gas-solid reactions that released H_2 and CO. As the carbon deposits were oxidised, the catalyst was gradually exposed to the surface and reacted with steam (R11) to produce high concentration of hydrogen, corresponding to 70–95 min in Fig. 3. There was only H_2 generated after 80 min, indicating that carbon has been consumed and only water splitting reaction occurred. Simultaneously, side reactions such as the water-gas shift (WGS) reaction and methanation reaction also occurred (R12-R15), with a small amount of CO_2 and CH_4 generated.

Stage-III was mainly the combustion of residual carbon deposits and

Table 2
The surface area and pore volume of different catalysts.

	Surface area[a] (m^2/g)	Total pore volume[b] (ml/g)	Average pore size [c] (nm)
Fresh	31.234	0.2326	29.7920
Stage-I	51.087	0.2528	19.7928
Stage-II	41.027	0.2275	22.1828
Stage-III	31.016	0.1674	21.5873

[a] Determined by BET method.
[b] Determined by BJH desorption total pore volume.
[c] Determined by BJH desorption average pore diameter.

the oxidation of iron compounds (R16-R17), and the oxygen carrier was regenerated through this stage. Overall, the sequential staging of the CLG process enables efficient separation and control of pyrolysis, reforming, and regeneration reactions. This design allows for maximised hydrogen yield, effective utilisation of the oxygen carrier, and minimisation of hydrocarbon by-products, highlighting the clear thermochemical and operational advantages of CLG over conventional gasification systems.

$$C + H_2O \rightarrow CO + H_2 \quad (R10)$$

$$3Fe + 4H_2O \rightarrow Fe_3O_4 + 4H_2 \quad (R11)$$

$$CO + H_2O \rightarrow CO_2 + H_2 \quad (R12)$$

$$2CO + 2H_2 \rightarrow CH_4 + CO_2 \quad (R13)$$

$$CO + 3H_2 \rightarrow CH_4 + H_2O \quad (R14)$$

$$CO_2 + 4H_2 \rightarrow CH_4 + 2H_2O \quad (R15)$$

$$C + O_2 \rightarrow CO_2 \quad (R16)$$

$$2Fe_3O_4 + (1/2)\ O_2 \rightarrow 3Fe_2O_3 \quad (R17)$$

The morphological changes of the oxygen carrier at different stages were observed by FE-SEM to further explain the mechanisms during the CLG process, as shown in Fig. 4. The block structure of different particle sizes, fluffy shapes and different pore structures can be observed in fresh oxygen carrier, indicating that the active components were well dispersed and effectively supported on the surface of aluminium in the Fe-Al oxygen carrier prepared via the impregnation method. After the stage-I reaction, sample exhibited a smaller particle size and a more developed pore structure due to the transfer of lattice oxygen and the decomposition of Fe_2O_3. BET data from Table 2 further confirmed that the average pore size of the sample decreased, while the specific surface area increased. Moreover, loose carbon deposits can be observed on the surface of the catalyst, the types of carbon are mainly divided into amorphous carbon, filamentous carbon and graphitic carbon [37]. Fig. 4 (b) illustrated that the carbon formed in this experiment was filamentous in nature, which, as reported in the literature, possesses certain catalytic properties [43]. During the stage-II reaction, the reduced iron species were partially oxidised by steam to form Fe_3O_4, thereby recovering part of lattice oxygen with the oxygen carrier. This redox transformation induced structural changes in the catalyst particles, notably particle enlargement due to oxygen uptake and associated volume expansion. In the final Stage-III, oxygen carrier was completely oxidised by air to recover the lattice oxygen and closing the redox cycle. Although minor agglomeration was observed, it still retained the porous structure, which was consistent with the initial crystal form and structure.

The evolution of crystalline phases in the oxygen carrier in different reaction stages were analysed by XRD as shown in Fig. S2. In the fresh catalyst sample, Fe_2O_3 and Al_2O_3 were mainly detected. During the stage-I reaction, stepwise reduction of Fe_2O_3 was observed with increasing temperature (R18) [44]. First, Fe_2O_3 was reduced to Fe_3O_4 at around 400 °C. This transition occurred rapidly and was accompanied by a high rate of lattice oxygen release, resulting in strong ability of oxidation and the generation of CO_2. As the temperature increased beyond 800 °C, further reduction of Fe_3O_4 to metallic Fe and FeO occurred. These two reactions occurred in parallel at higher temperature (above 800 °C), and the oxidation capacity of the catalyst was weak at this time [45]. Due to the abundant pyrolysis gas reacting with the catalyst, Fe_2O_3 was ultimately reduced to metallic Fe, while Al_2O_3 only provided catalyst support and did not participate in the reaction. It was worth noting that the diffraction peak of carbon was detected at about 26°, which is consistent with the result of SEM observation. Following the stage-II reaction, partial reoxidation of Fe to Fe_3O_4 was detected, in accordance with the limited oxidising strength of steam. Additionally, the diffraction peak of Fe-Al was also discovered, indicating that although Al_2O_3 did not participate in the reaction, the reactivity of catalyst can be improved through metal synergistic effect. During the air oxidation stage, complete reoxidation of the oxygen carrier restored the lattice oxygen content. Importantly, the catalyst retained its original crystalline structure, confirming its phase stability and robustness under repeated redox cycling.

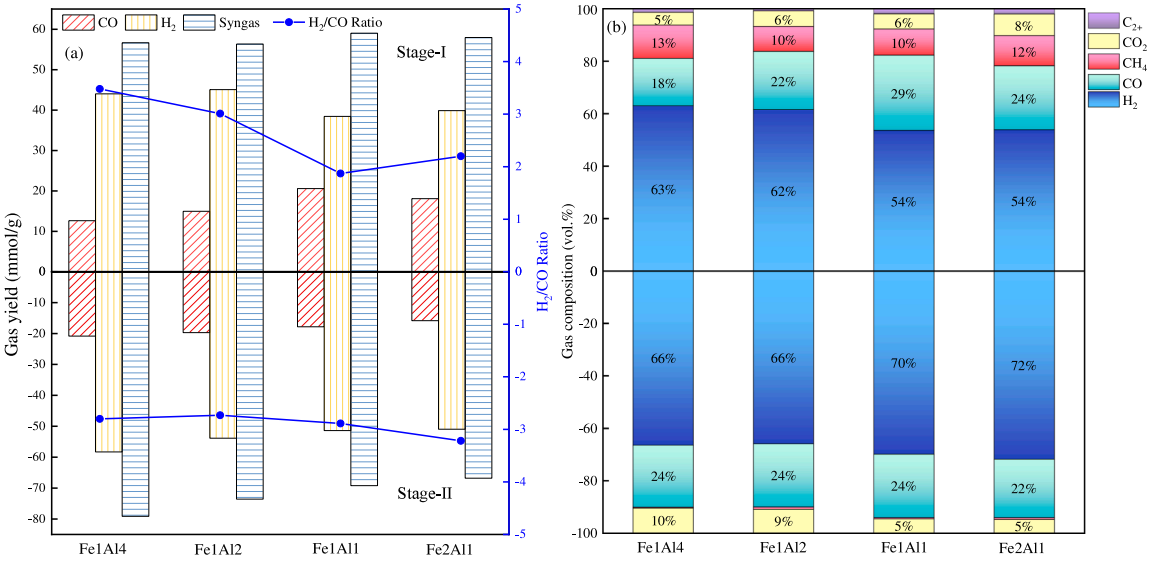

Fig. 5. The effect of different ratios of Fe to Al on gas products in stage-I and stage-II: (a) gas yield, (b) gas composition.

Table 3
Effect of different Fe to Al ratios on products.

	Catalyst	Fe1Al4	Fe1Al2	Fe1Al1	Fe2Al1
Stage-I	Liquid yield, wt. %	10.73	2.28	5.62	5.59
	Carbon yield[1], wt. %	23.75	33.53	7.30	3.84
	Gas yield, wt. %	75.99	79.46	99.00	103.64
Stage-II	Liquid yield, wt. %	27.10	28.28	21.80	26.47
	Carbon yield[1], wt. %	0.60	0.30	0.10	0.10
	Gas yield, wt. %	53.86	50.35	39.41	35.91

[1] In relation to catalyst.

$$Fe_2O_3 \rightarrow Fe_3O_4 \rightarrow Fe/FeO \quad (R18)$$

3.3. Effect of Fe to Al ratio on CLG performance

To understand the outstanding performance of hydrogen/syngas production in the CLG process, the impact of oxygen carriers with varying molar ratios of Fe to Al on different stages was researched. It can be seen from Fig. S2 that the XRD results of fresh oxygen carrier generally agree with the preparation rules of catalysts with different Fe to Al ratios. Fig. 5 shows the effect of different Fe to Al ratios on gas products, including gas yield, composition, and H_2/CO ratio in both stage-I and stage-II. Results manifested that the yield and composition of H_2 displayed a decreasing trend as the ratio of Fe to Al increased in stage-I, the lowest volumes were 38.44 mmol/$g_{plastic}$ and 53.62 vol % when Fe to Al ratio was 1. Conversely, the yield and composition of CO gradually climbed, reaching the maximum of 20.59 mmol/$g_{plastic}$ and 28.72 vol %. This trend was similarly reflected in CO selectivity (defined by R3), which peaked at 83.15 % when the Fe to Al ratio was 1. The H_2/CO ratio decreased significantly from 3.48 (Fe1Al4) to 1.87 (Fe1Al1), indicating a 46 % reduction. Moreover, the concentration of CO_2 raised by degree, reaching 8.22 vol % in Fe2Al1. And the concentrations of CH_4 and C_{2+} were the lowest in Fe1Al2, which were 9.53 vol % and 0.78 vol %.

With the augment of Fe content, the lattice oxygen content supply increased accordingly, contributing to the enhanced generation of CO and CO_2. When Fe to Al ratio rose from 1 to 2, excess oxygen oxidised C atoms into CO_2, resulting in lower CO yield. When Fe to Al ratio increased from 0.25 to 0.5, more metallic iron was generated, which promoted the secondary cracking of hydrocarbons. Therefore, both the yield and concentration of H_2 increased, while the concentration of CH_4 and C_{2+} decreased, accompanied by a corresponding reduction in detected liquid production (Table 3). As for Fe1Al1 and Fe2Al1, the content of iron further increased, but the effect of iron dispersion on the support became worse because of the unchanged aluminium content. The degradation of catalytic performance was attributed to the increased susceptibility of the oxygen carrier to sintering and agglomeration at high temperatures. Simultaneously, the increased formation of CO and CO_2 enhanced the methanation reaction (R13-R15), leading to a higher consumption of H_2 in the presence of the oxygen carrier.

As shown in Fig. 5, gas products in stage-II were mainly H_2 and CO, although a small amount of CO_2 was generated, the purity of the syngas produced in this stage was as high as 90 %, or even higher. The yield of H_2 decreased with the increase of Fe to Al ratio. Even though more Fe_2O_3 was reduced in the first stage, according to the reaction formula R11, a higher iron content in the catalyst would theoretically result in more metallic Fe participating in the steam reforming reaction, thereby producing more H_2. However, under low Fe to Al ratio conditions, more mixed oxides between iron and aluminium species as shown in Fig. 6(d). This synergistic interaction improved the thermochemical properties of the oxygen carrier and the transmission capacity of lattice oxygen

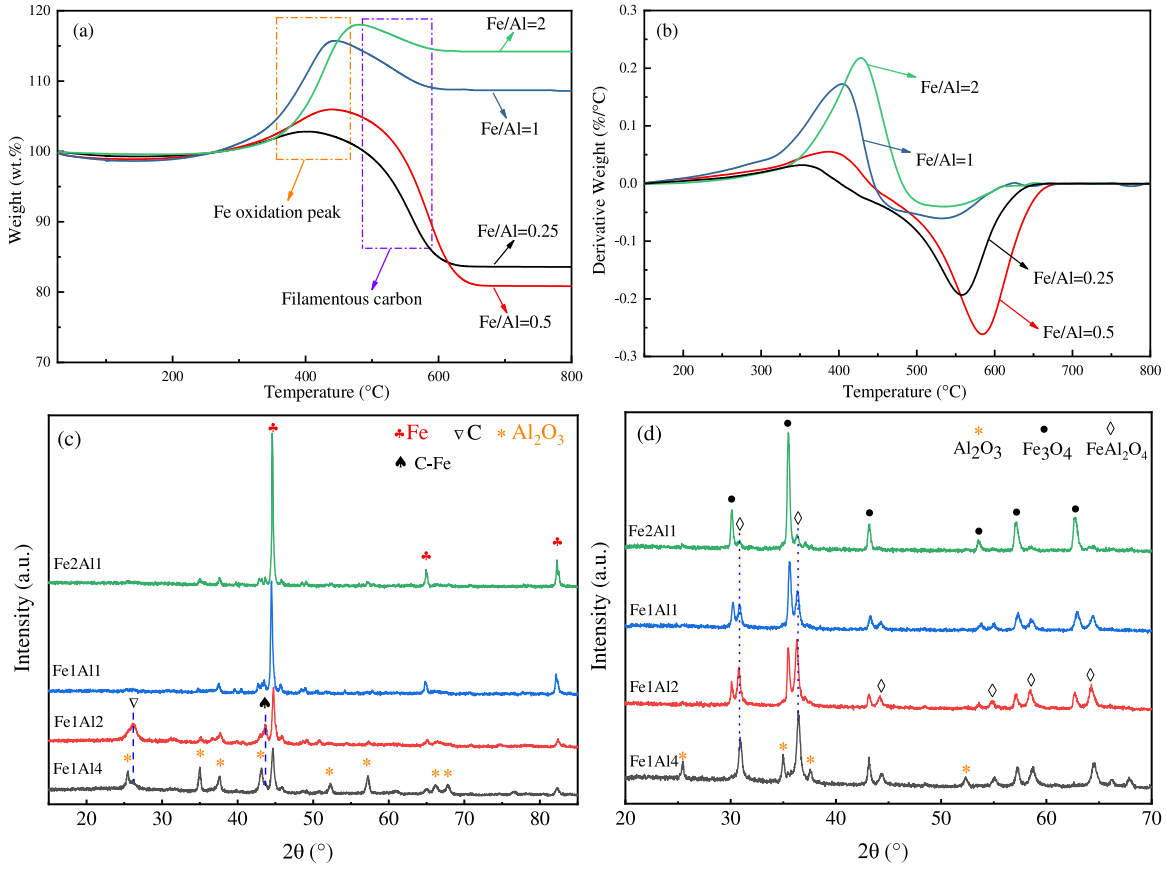

Fig. 6. TPO and XRD results of different Fe to Al ratio catalysts: (a), (b) TPO and its derivative curve in first stage; (c), (d) XRD results in different stages.

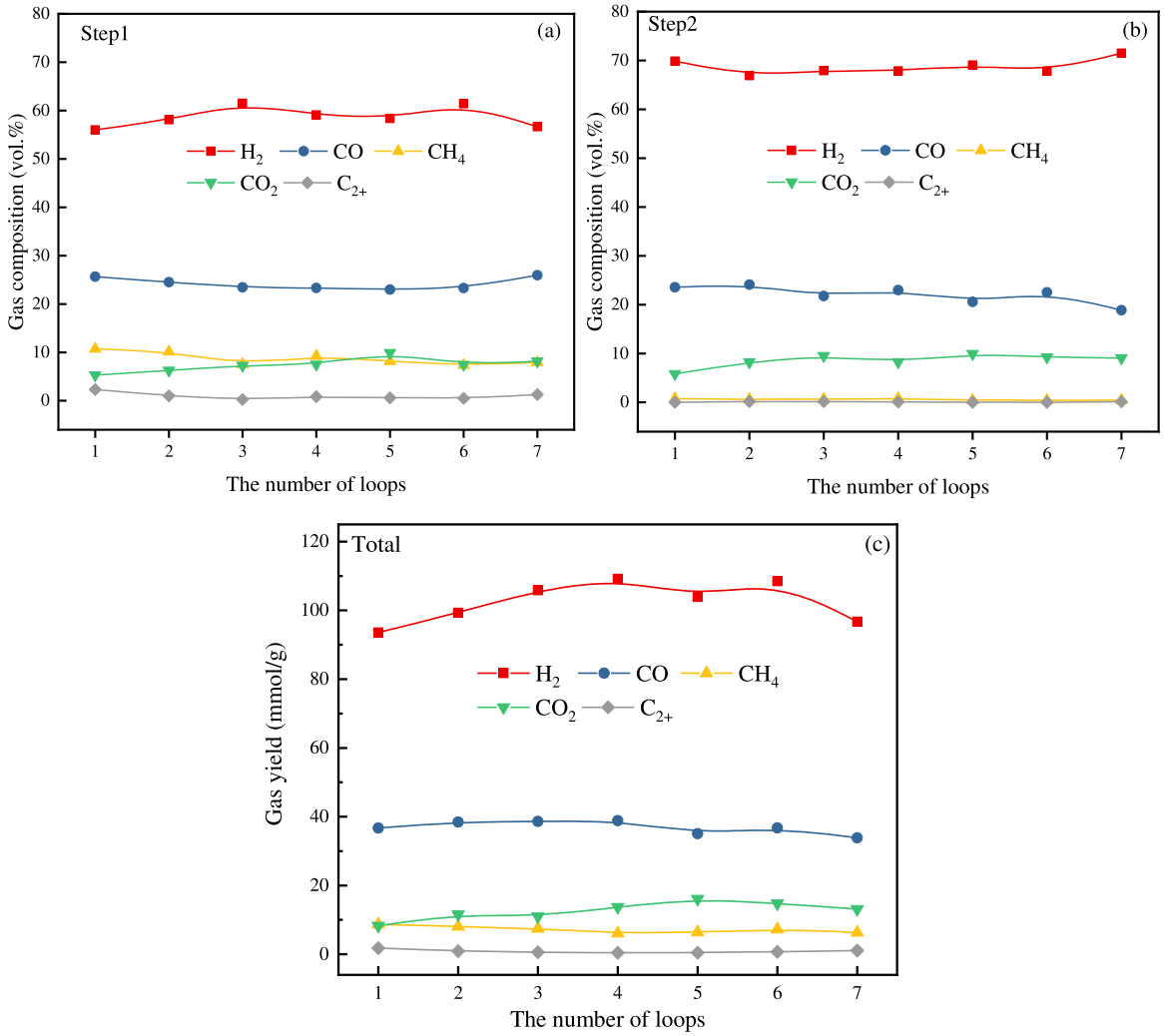

Fig. 7. Gas yield and composition in the cyclic experiment.

during the entire reaction. However, the catalytic performance of oxygen carrier was weaken under high Fe to Al ratios, possibly because some iron species may not participate in the steam reforming reaction [46]. Furthermore, since a large amount of carbon deposition was oxidised by the lattice oxygen provided by Fe_2O_3 during the first stage, the overall carbon deposition content was reduced. As a result, H_2, CO, and CO_2 produced by the gasification of carbon deposits in stage-II were correspondingly decreased, while the H_2/CO ratio stabilised at approximately 2.91.

TPO analysis was also performed to investigate the deposition of carbon on the catalyst and thermal stability of spent oxygen carriers. The amount of carbon deposits was found to be <1 wt. % due to the reaction between carbon and steam in stage-II. Fig. 6(a) and (b) show the weight loss diagram of the stage-I. It can be seen that the oxidation process of spent catalyst consisted of two stages: 200–450 °C corresponded to the oxidation of Fe to Fe_2O_3 and the coke combustion was after 450 °C [13]. The maximum weight gain of 18.41 wt. % was obtained in Fe2Al1. This was because more metallic Fe was oxidised as the content of iron increased. The amount of charcoal deposition was calculated according to the weight loss of oxygen carrier from 450 °C (when the carbon deposits began to oxidise after iron was completely oxidised) to 800 °C and the results were shown in Table 3. The maximum solid carbon yield of 33.53 wt. % was obtained when the Fe to Al ratio was 0.5, suggesting that the secondary cracking of hydrocarbons was most effective under this condition. This finding is supported by the lowest content of C_{2+} in Fig. 5(b). Since most of carbon was oxidised by the lattice oxygen, less carbon was detected in Fe1Al1and Fe2Al1. The trend of carbon deposit was consistent with the trends observed in the gas products described earlier. The corresponding carbon oxidation peak in the derivative weight graph in Fig. 6(b) indicated that the peak was concentrated at a relatively high temperature (550 °C-600 °C), thus the carbon production in this reaction was assigned to the filamentous carbon [47]. This type of carbon deposition identified by TPO aligned well with the morphology observed by SEM imaging (Fig. 4b).

Fig. 6(c) and (d) show the XRD spectra of spent oxygen carrier with different Fe to Al ratios in stage-I and stage-II. In the first stage, the sharp diffraction lines observed in samples were assigned to metallic Fe, with no other iron crystal phases detected, indicating that Fe_2O_3 was nearly fully reduced by the volatiles generated by the pyrolysis of feedstock. Notably, distinct carbon diffraction peaks can be detected when the ratio of Fe to Al was 0.25 and 0.5, while these carbon peaks weaken or even disappeared as iron content increased. This indicated that the oxygen carrier with lower iron content had better catalytic cracking performance, effectively decomposing macromolecular compounds into more carbon and small molecule gas. However, a higher content of Fe provided more lattice oxygen to oxidise the carbon. These observations further confirmed TPO results.

In stage-II, Fe_3O_4 and $FeAl_2O_4$ were mainly detected in spent oxygen carrier, corresponding to the partial oxidation of iron by steam. Lower iron loading was associated with stronger Fe-Al diffraction peaks, which correspond to mixed oxides with a spinel structure known to enhance catalyst activity and stability [36]. The formation of this spinel phase

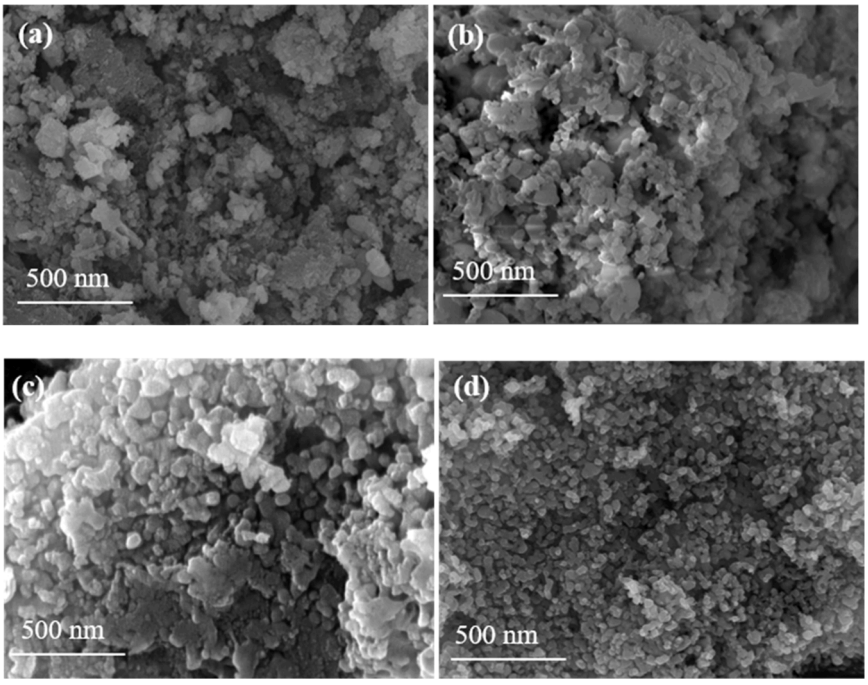

Fig. 8. Cycle performance of oxygen carrier: (a) SEM image of fresh oxygen carrier, (b)~(d) SEM images of oxygen carriers after several redox cycles: (b) 1st cycle after air oxidation, (b) 4th cycle (d) 7th cycle.

played a crucial in stabilising Fe species within a thermally robust matrix, thereby inhibiting particle agglomeration and sintering during redox cycling. Moreover, lattice oxygen mobility was facilitated by the spinel structure due to its inherent oxygen vacancies and strong metal-oxygen bonding, enhancing oxygen transfer during the gasification process. These attributes improving both redox efficiency and long-term catalyst stability. For the higher Fe content of oxygen carriers, iron was primarily oxidised to Fe_3O_4. Although the catalyst can provide more lattice oxygen under this circumstance, the catalytic performance of the oxygen carrier was diminished due to poor iron dispersion on the support.

Table 4
BET surface area and pore structure of fresh and spent catalysts after different cycles.

	Surface area (m^2/g)	Total pore volume (ml/g)	Average pore size (nm)
Fresh	31.234	0.2326	29.7920
1st cycle	31.016	0.1674	21.5873
4th cycle	21.678	0.1340	24.7247
7th cycle	14.808	0.0871	23.5319

3.4. Cycle performance

The cyclic stability is a key indicator for evaluating CLG performance. Based on the reaction performance of oxygen carriers with different ratios, seven sets of redox cycle experiments were conducted in the fixed bed reactor using Fe1Al2. As shown in Fig. 7(a) and (b), the concentration of gas products remained stable at each stage during the experiment. In stage-I, the concentration of H_2 was maintained at about 58.73 vol %, while CO, CH_4 and CO_2 concentrations were steady at 24.17 vol %, 8.73 vol % and 7.41 vol %, respectively. The concentration of C_{2+} was below 1 vol %. In stage-II, the main gas components were H_2, CO and CO_2, accounting for 68.70 vol %, 22.06 vol % and 8.59 vol %, respectively, with CH_4 and C_{2+} being nearly undetectable. In addition, the total yield of each gas in every cycle experiment was calculated in line with the laboratory measurements. As shown in the Fig. 7(c), the gas yield remained stable with the increasing cycle number, and the output of H_2 output even showed a slight increased. A single cycle produced 101.09 mmol/$g_{plastic}$ H_2 and 36.49 mmol/$g_{plastic}$ CO, resulting in a total syngas yield of approximately 137.59 mmol/$g_{plastic}$. These results indicated that Fe1Al2 maintains outstanding reactivity and cycle stability throughout multiple redox cycles.

The oxygen carriers regenerated in the 1st, 4th, and 7th cycles were examined. Fig. 8 shows the changes in its morphology and crystalline composition throughout the entire cycling experiment. As shown in Fig. 8(b), after one cycle regeneration, the oxygen carrier maintained a loose and porous structure. However, with an increasing number of cycles, partial agglomeration occurred, causing the oxygen carrier to become denser and more compact (Fig. 8(c)-(d)). This behaviour may be

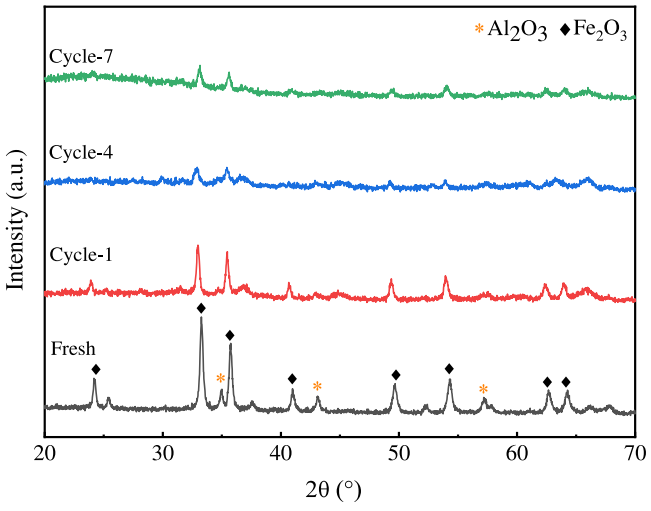

Fig. 9. XRD analysis for catalysts after cycles.

attributed to the sintering of Fe_2O_3 during the reaction [48]. Sintering is fundamentally a diffusion-limited process of metal cations that leads to the agglomeration of iron particles. Although it reduced surface area and pore volume (Table 4), it did not significantly alter the total oxygen storage capacity or eliminate all available active sites [49], as evidenced by the preserved porous morphology and stable syngas yield across cycles.

XRD spectra in Fig. 9 demonstrates that the oxygen carrier retained its primary crystal phases after 7 cycles. In the presence of inert components (Al_2O_3), the sintering of oxygen carrier particles and the detachment of active components (Fe) can be effectively inhibited, thereby maintaining the cycle stability [30]. However, with the increase of the number of cycles, the intensity of Fe_2O_3 diffraction peak dropped, indicating that some iron species failed to fully deoxidise to Fe_2O_3 after air oxidation. The spinel was only partially recovered from the repeatedly reduction from Fe_2O_3 to Fe_3O_4. However, this impact on active oxygen availability appeared minimal within 7 cycles, as supported by the consistent gas production results.

Furthermore, the BET surface area and pore structure of the oxygen carrier after different cycles were listed in Table 4. As the number of cycle increased, the specific surface area and total pore volume of the oxygen carrier decreased, indicating that there was partial sintering of the oxygen carrier during the cycle process. However, the average pore size of different oxygen carrier remained stable. These results, together with SEM and XRD analyses, suggested that while sintering occurred, it did not severely compromise the oxygen carrier's functionality. The catalyst maintained high reactivity and sufficient active sites for oxygen transfer even after 7 cycles.

4. Conclusion

The staged chemical looping gasification of waste plastics with enhanced production of hydrogen-rich syngas was investigated in this work. The main conclusions are summarised as follows:

(1) Compared to traditional gasification, the staged CLG process significantly increased the yield of hydrogen-rich syngas by 31.53 %, with promoted catalytic decomposition and steam reforming reactions. The higher H_2/CO ratio (from 2.68 to 2.75) further indicates the improved syngas quality from intensified water-gas shift reaction.
(2) The first stage of the CLG process included three main steps: initial pyrolysis, oxygen carrier reduction, and metallic Fe activation. For the second stage, the hydrogen concentration was further enhanced by introducing steam. The third stage involved air oxidation, which regenerated the oxygen carrier and restored its original crystalline structure.
(3) Fe-Al with a spinel structure were favoured under low iron loading conditions, improving the thermochemical properties of the oxygen carrier and improving the lattice oxygen transfer capacity throughout the reaction. While a high Fe content provided more lattice oxygen to oxidise carbon, the catalytic performance was diminished due to poor dispersion of active components on the support.
(4) The Fe1Al2 oxygen carrier promoted as high as 101.09 mmol/$g_{plastic}$ of H_2 and 137.59 mmol/$g_{plastic}$ of syngas, and maintained excellent reactivity and cyclic stability. Although slight agglomeration and sintering were observed, they did not significantly compromise performance but may need further modifications. Future work will focus on the rational design of oxygen carriers with improved thermal resistance and structural stability, to further enhance long-term performance in muti-cycle operations.

CRediT authorship contribution statement

Zongqiang Ren: Writing – original draft, Methodology, Investigation. **Zhenghui Gao:** Visualization, Methodology. **Zhenliang Guo:** Visualization, Methodology. **Peiwen Liu:** Writing – review & editing. **Dingding Yao:** Writing – review & editing, Supervision, Funding acquisition, Conceptualization.

Declaration of competing interest

The authors declare that they have no known competing financial interests or personal relationships that could have appeared to influence the work reported in this paper.

Acknowledgements

The authors gratefully acknowledge the financial support by National Natural Science Foundation of China (52106150) and Fundamental Research Funds for the Central Universities.

Supplementary materials

Supplementary material associated with this article can be found, in the online version, at doi:10.1016/j.jaecs.2025.100362.

Data availability

Data will be made available on request.

References

[1] Nayanathara Thathsarani Pilapitiya PGC, Ratnayake AS. The world of plastic waste: a review. Clean Mater 2024;11:100220. https://doi.org/10.1016/j.clema.2024.100220.
[2] Taqi HMM, Salman S, Ahmed S, Taghipour A, Mazumder N, Ali SM. Plastic waste reduction through catalyzing motivational factors: implications for sustainable development goals in emerging economies. Sustain Fut 2025;9:100657. https://doi.org/10.1016/j.sftr.2025.100657.
[3] Idowu GA, Oriji AY, Olorunfemi KO, et al. Why Nigeria should ban single-use plastics: excessive microplastic pollution of the water, sediments and fish species in Osun River, Nigeria. J Hazard Mater Adv 2024;13:100409. https://doi.org/10.1016/j.hazadv.2024.100409.
[4] Benson NU, Bassey DE, Palanisami T. COVID pollution: impact of COVID-19 pandemic on global plastic waste footprint. Heliyon 2021;7(2):e06343. https://doi.org/10.1016/j.heliyon.2021.e06343.
[5] Jie X, Li W, Slocombe D, et al. Microwave-initiated catalytic deconstruction of plastic waste into hydrogen and high-value carbons. Nat Catal 2020;3(11):902–12. https://doi.org/10.1038/s41929-020-00518-5.
[6] Jung S, Lee S, Dou X, Kwon EE. Valorization of disposable COVID-19 mask through the thermo-chemical process. Chem Eng J 2020;405:126658.
[7] Wu S, Ren Z, Hu Q, Yao D, Yang H. Upcycling plastic waste into syngas by staged chemical looping gasification with modified Fe-based oxygen carriers. Appl Energy 2024;353:122105. https://doi.org/10.1016/j.apenergy.2023.122105.
[8] Shi X, Chen Z, Wei W, Ni B-J. Perspectives on sustainable plastic treatment: a shift from linear to circular economy. TrAC Trends Analy Chem 2024;173:117631. https://doi.org/10.1016/j.trac.2024.117631.
[9] Ruoppolo G, Ammendola P, Chirone R, Miccio F. H2-rich syngas production by fluidized bed gasification of biomass and plastic fuel. Waste Manag 2012;32(4):724–32. https://doi.org/10.1016/j.wasman.2011.12.004.
[10] Barco-Burgos J, Carles-Bruno J, Eicker U, Saldana-Robles AL, Alcántar-Camarena V. Hydrogen-rich syngas production from palm kernel shells (PKS) biomass on a downdraft allothermal gasifier using steam as a gasifying agent. Energy Convers Manag 2021;245:114592. https://doi.org/10.1016/j.enconman.2021.114592.
[11] Sadeq AM, Homod RZ, Hussein AK, et al. Hydrogen energy systems: technologies, trends, and future prospects. Sci Total Environ 2024;939:173622. https://doi.org/10.1016/j.scitotenv.2024.173622.
[12] Wang Z, Burra KG, Li X, et al. CO2-assisted gasification of polyethylene terephthalate with focus on syngas evolution and solid yield. Appl Energy 2020;276:115508. https://doi.org/10.1016/j.apenergy.2020.115508.
[13] Yao D, Yang H, Chen H, Williams PT. Co-precipitation, impregnation and so-gel preparation of Ni catalysts for pyrolysis-catalytic steam reforming of waste plastics. Appl Cataly B: Environ 2018;239:565–77. https://doi.org/10.1016/j.apcatb.2018.07.075.
[14] Saxena S. Pyrolysis and beyond: sustainable valorization of plastic waste. Appl Energy Combust Sci 2025;21:100311. https://doi.org/10.1016/j.jaecs.2024.100311.
[15] Barbarias I, Artetxe M, Lopez G, et al. Catalyst performance in the HDPE pyrolysis-reforming under reaction-regeneration cycles. Catalysts 2019;9:414. https://doi.org/10.3390/catal9050414.

[16] Dou B, Wang K, Jiang B, et al. Fluidized-bed gasification combined continuous sorption-enhanced steam reforming system to continuous hydrogen production from waste plastic. Int J Hydrogen Energy 2016;41(6):3803–10. https://doi.org/10.1016/j.ijhydene.2015.12.197.
[17] Saad JM, Williams PT. Pyrolysis-catalytic dry (CO2) reforming of waste plastics for syngas production: influence of process parameters. Fuel 2017;193:7–14. https://doi.org/10.1016/j.fuel.2016.12.014.
[18] Yao D, Yang H, Chen H, Williams PT. Investigation of nickel-impregnated zeolite catalysts for hydrogen/syngas production from the catalytic reforming of waste polyethylene. Appl Cataly B: Environ 2018;227:477–87. https://doi.org/10.1016/j.apcatb.2018.01.050.
[19] Wang Z, Gong Z, Turap Y, Wang Y, Zhang Z, Wang W. Renewable hydrogen production from biogas using iron-based chemical looping technology. Chem Eng J 2022;429:132192. https://doi.org/10.1016/j.cej.2021.132192.
[20] Shang Q, Feng D, Zhang X, et al. Synergistic effects of biomass/plastics and multi-step regulation of H2O in the co-production of H2-CNTs by gasification of biomass and plastic wastes. Appl Cataly B: Environ Energy 2025;379:125695. https://doi.org/10.1016/j.apcatb.2025.125695.
[21] Goel A, Moghaddam EM, Liu W, He C, Konttinen J. Biomass chemical looping gasification for high-quality syngas: a critical review and technological outlooks. Energy Convers Manag 2022;268:116020. https://doi.org/10.1016/j.enconman.2022.116020.
[22] Guo F, Li X, Liu Y, Peng K, Guo C, Rao Z. Catalytic cracking of biomass pyrolysis tar over char-supported catalysts. Energy Convers Manag 2018;167:81–90. https://doi.org/10.1016/j.enconman.2018.04.094.
[23] Hu J, Li C, Guo Q, et al. Syngas production by chemical-looping gasification of wheat straw with Fe-based oxygen carrier. Bioresour Technol 2018;263:273–9. https://doi.org/10.1016/j.biortech.2018.02.064.
[24] Yang J, Dong S, Xie L, et al. Analysis of hydrogen-rich syngas generation in chemical looping gasification of lignite: application of carbide slag as the oxygen carrier, hydrogen carrier, and in-situ carbon capture agent. Energy 2023;283:128499. https://doi.org/10.1016/j.energy.2023.128499.
[25] Zhang K, Zhang Q. Evaluation of Fe-Ni composite oxygen carrier in coal chemical looping gasification. Int J Energy Res 2024;2024(1):9252190.
[26] Gao Z, Hong S, Yin F, et al. Enhanced hydrogen production and fuel conversion of an iron-based oxygen carrier in the chemical looping process by a small co-addition of CuO and NiO. J Mater Chem A 2025.
[27] Yao D, Yang H, Hu Q, Chen Y, Chen H, Williams PT. Carbon nanotubes from post-consumer waste plastics: investigations into catalyst metal and support material characteristics. Appl Cataly B: Environ 2021;280:119413. https://doi.org/10.1016/j.apcatb.2020.119413.
[28] Niu Y, Chi Z, Li M. Advancements in biomass gasification research utilizing iron-based oxygen carriers in chemical looping: a review. Mater Rep: Energy 2024;4(3):100282. https://doi.org/10.1016/j.matre.2024.100282.
[29] Dou B, Wu K, Zhang H, Chen B, Chen H, Xu Y. Sorption-enhanced chemical looping steam reforming of glycerol with CO2 in-situ capture and utilization. Chem Eng J 2023;452:139703. https://doi.org/10.1016/j.cej.2022.139703.
[30] Huang Z, Deng Z, Chen D, et al. Exploration of reaction mechanisms on hydrogen production through chemical looping steam reforming using NiFe2O4 oxygen carrier. ACS Sustain Chem Eng 2019;7(13):11621–32. https://doi.org/10.1021/acssuschemeng.9b01557.
[31] Mahmoudi E, Sayyah A, Farhoudi S, et al. Advances in catalysts for direct syngas conversion to light olefins: a review of mechanistic and performance insights. J CO2 Utiliz 2024;86:102893. https://doi.org/10.1016/j.jcou.2024.102893.
[32] Chen X, Wang L, Lin Y, et al. Migration of lattice oxygen during chemical looping dry reforming of methane with Ca2Fe2O5/Zr0.5Ce0.5O2 oxygen carrier. Fuel Proc Technol 2023;244:107706. https://doi.org/10.1016/j.fuproc.2023.107706.
[33] Kang K-S, Kim C-H, Bae K-K, Cho W-C, Kim S-H, Park C-S. Oxygen-carrier selection and thermal analysis of the chemical-looping process for hydrogen production. Int J Hydrogen Energy 2010;35(22):12246–54. https://doi.org/10.1016/j.ijhydene.2010.08.043.
[34] Ma Z, Liu G, Lu Y, Zhang H. Redox performance of Fe2O3/Al2O3 oxygen carrier calcined at different temperature in chemical looping process. Fuel 2021:122381. https://doi.org/10.1016/j.fuel.2021.122381.
[35] Galvita V, Hempel T, Lorenz H, Rihko-Struckmann LK, Sundmacher K. Deactivation of modified iron oxide materials in the cyclic water gas shift process for CO-free hydrogen production. Ind Eng Chem Res 2008;47(2):303–10. https://doi.org/10.1021/ie0708879.
[36] Dharanipragada NVRA, Buelens LC, Poelman H, De Grave E, Galvita VV, Marin GB. Mg–Fe–Al–O for advanced CO2 to CO conversion: carbon monoxide yield vs. oxygen storage capacity. J Mater Chem A 2015;3(31):16251–62. https://doi.org/10.1039/C5TA02289D.
[37] Zhu M, Song Y, Chen S, Li M, Zhang L, Xiang W. Chemical looping dry reforming of methane with hydrogen generation on Fe2O3/Al2O3 oxygen carrier. Chem Eng J 2019;368:812–23. https://doi.org/10.1016/j.cej.2019.02.197.
[38] Yao D, Wu C, Yang H, et al. Co-production of hydrogen and carbon nanotubes from catalytic pyrolysis of waste plastics on Ni-Fe bimetallic catalyst. Energy Convers Manag 2017;148:692–700. https://doi.org/10.1016/j.enconman.2017.06.012.
[39] Wu Y, Ye X, Wang Y, Wang L. Methane production from biomass by thermochemical conversion: a review. Catalysts 2023;13(4):771.
[40] Lazzarotto IP, Ferreira SD, Junges J, et al. The role of CaO in the steam gasification of plastic wastes recovered from the municipal solid waste in a fluidized bed reactor. Process Safety Environ Protect 2020;140:60–7. https://doi.org/10.1016/j.psep.2020.04.009.
[41] Falascino E, Joshi RK, Kumar S, et al. Enabling plastic waste gasification by autothermal chemical looping with >90 % syngas purity for versatile feedstock handling. Appl Energy Combust Sci 2024;19:100270. https://doi.org/10.1016/j.jaecs.2024.100270.
[42] Zhong D, Zeng K, Li J, et al. Characteristics and evolution of heavy components in bio-oil from the pyrolysis of cellulose, hemicellulose and lignin. Renew Sustain Energy Rev 2022;157:111989. https://doi.org/10.1016/j.rser.2021.111989.
[43] Yao D, Hu Q, Wang D, et al. Hydrogen production from biomass gasification using biochar as a catalyst/support. Bioresour Technol 2016;216:159–64. https://doi.org/10.1016/j.biortech.2016.05.011.
[44] Al-Dossary M, Fierro JLG. Effect of high-temperature pre-reduction in Fischer–Tropsch synthesis on Fe/ZrO2 catalysts. Appl Cataly A: Gen 2015;499:109–17. https://doi.org/10.1016/j.apcata.2015.03.031.
[45] Chen H, Zheng Z, Chen Z, Bi XT. Reduction of hematite (Fe2O3) to metallic iron (Fe) by CO in a micro fluidized bed reaction analyzer: a multistep kinetics study. Powder Technol 2017;316:410–20. https://doi.org/10.1016/j.powtec.2017.02.067.
[46] Wei G, Huang J, Fan Y, et al. Chemical looping reforming of biomass based pyrolysis gas coupling with chemical looping hydrogen by using Fe/Ni/Al oxygen carriers derived from LDH precursors. Energy Convers Manag 2019;179:304–13. https://doi.org/10.1016/j.enconman.2018.10.065.
[47] Yao D, Li H, Dai Y, Wang C-H. Impact of temperature on the activity of Fe-Ni catalysts for pyrolysis and decomposition processing of plastic waste. Chem Eng J 2021;408:127268. https://doi.org/10.1016/j.cej.2020.127268.
[48] Hu Q, Shen Y, Chew JW, Ge T, Wang C-H. Chemical looping gasification of biomass with Fe2O3/CaO as the oxygen carrier for hydrogen-enriched syngas production. Chem Eng J 2020;379:122346. https://doi.org/10.1016/j.cej.2019.122346.
[49] Datta P, Rihko-Struckmann LK, Sundmacher K. Influence of molybdenum on the stability of iron oxide materials for hydrogen production with cyclic water gas shift process. Mater Chem Phys 2011;129(3):1089–95. https://doi.org/10.1016/j.matchemphys.2011.05.066.